Title

- Synapse profiling of identified neurons in the *Drosophila* brain.

Authors

[1] Hongyang Wu, [2] Yoh Maekawa, [1] Sayaka Eno, [3] Shu Kondo, [4] Nobuhiro Yamagata, [1,2]* Hiromu Tanimoto

Affiliations

[1] Graduate School of Life Sciences, Tohoku University, Sendai, Japan.
[2] Department of Biology, Faculty of Science, Tohoku University, Sendai, Japan.
[3] Department of Biological Science and Technology, Tokyo University of Science, Tokyo, Japan.
[4] Department of Life Science, Graduate School of Engineering Science, Akita, Akita University.
* Correspondence: Dr. Hiromu Tanimoto (hiromut@m.tohoku.ac.jp)

Abstract

Synapses are highly heterogeneous even within a single motor neuron in *Drosophila melanogaster*. In the central nervous system (CNS), the degree of stereotypy in the synaptic structure of specific neurons across individuals remains largely unexplored, due to the significant effort required to analyze multiple brain samples. Utilizing the split-GFP fluorescence-tagging, we achieved endogenous labeling of the presynaptic active zone (AZ) scaffold protein Bruchpilot (Brp) in a cell-type-specific manner. This strategy allowed us to devise a high-throughput quantification pipeline to characterize and compare cell-type-specific AZ structures across individuals. We found that multiple structural parameters such as Brp localization and AZ size revealed significant intracellular synaptic heterogeneity and cell-type-dependent stereotypy in the mushroom body (MB) circuit. Furthermore, we found that the AZ organization can be surprisingly local, even at the neighboring AZ level. These findings therefore suggest multi-level organizations of AZs, from neighboring synapses to across individuals.

Teaser

State-of-art fluorescence-based imaging technique and high-throughput analysis revealed previously unidentified synaptic organizations.

Introduction

The nanoscopic organization of presynaptic AZs is highly heterogeneous, even within a single *Drosophila* motor neuron (*1*, *2*). The AZ scaffold protein Brp accumulates differentially at individual AZs, determining the characteristics of synaptic vesicle release (*2–8*). Brp forms the electron-dense projections decorating AZs in the electron microscopy images. Leveraging Brp as a marker, individual synaptic connections have been systematically mapped in Drosophila CNS, enabling the construction of brain connectomes (*9–13*). However, the low throughput of connectome-based approaches limits their application to large sample sets. Since the synaptic structure and connectivity reflect substantial variability of development and experiences (*14–19*), cross-individual comparisons are necessary. Fluorescence labeling offers high-throughput when handling a large sample set. Nevertheless, characterizing endogenous synapses in specific cells using fluorescence-labeling remains challenging due to the dense intermingling of synapses

from different neurons in the CNS. This has driven growing interest in designing cell-type-specific fluorescence-tagging strategies for endogenous synaptic protein (*20*).

The circuit of *Drosophila* MBs plays a central role in olfactory associative learning (*21*). The intrinsic MB neuron, known as Kenyon cells (KCs) respond to odor stimulation and synapse onto the spatially segregated dendrites of MB output neurons (MBONs). These dendrites of MBON therefore divide the MB into compartments. Distinct types of dopamine neurons (DANs) respond to reward or punishment signals, terminating in specific compartments and regulating their synaptic activities. This compartmentalization allows the MB to function as a set of isolated modules during olfactory learning (*22*). Two functionally distinct interneurons, the anterior paired lateral neuron (APL) and the dorsal paired medial (DPM) neuron extensively ramify across the MB lobes and provide recurrent modulations to KC synapses (*23–30*). However, the dense packing of synapses in the MB has made it difficult to characterize the detailed synaptic structures of specific MB neurons.

Here, we present a spatial analysis of individual AZs within the MB circuit at single-cell resolution, achieved by cell-type-specific visualization of endogenous Brp using the CRISPR/Cas9-mediated split-GFP tagging system. We developed a quantification pipeline to systematically profile Brp clusters of individual AZs in MB neurons. Characterizing multiple structural parameters revealed a significant synaptic heterogeneity within single neurons and AZ distribution stereotypy across individuals. These cell-type-specific synapse profiles suggest that AZs are organized at multiple levels, ranging from neighboring synapses to across individuals.

Results

Establishing an experimental system for cell-type-specific profiling of active zone structures

To visualize endogenous Brp in designated cell types, we employed a CRISPR/Cas9-mediated split-GFP tagging system. Using CRISPR/Cas9, we inserted the GFP11 fragment (the eleventh β-strand of the super-folder GFP) just prior to the stop codon of *brp* gene. The GFP1-10 fragment is expressed cell-type-specifically by the GAL4/UAS system. The self-assembly of GFP therefore occurs only in cells expressing GAL4 (Fig. 1A). We directed the GFP reconstitution and expressed plasma membrane marker in the single serotonergic neuron, DPM neuron using VT64246-GAL4 (Fig. 1B). Confocal microscopy revealed Brp::reconstituted GFP (Brp::rGFP) signals only to the MB lobes, matching the location of DPM axon terminals (*30*). These signals appear as puncta with plasma membrane swellings resembling presynaptic boutons (Fig. 1B), suggesting that Brp::rGFP clusters labeled individual AZs in DPM neuron.

To systematically profile Brp::rGFP clusters, we developed an image processing pipeline (Fig. 2A). In brief, image deconvolution was applied to reduce out-of-focus light and enhance signal sharpness. Individual Brp::rGFP clusters were then segmented using the 3D suite plugin in Fiji (*31*), generating the 3D region-of-interests (3D ROIs) that encircle each cluster. We measured the Brp::rGFP signal intensity, volume and location of individual clusters using the 3D ROIs. To optimize the segmentation, we systematically varied the parameters and calculated the F-score to measure the error rates (see MATERIALS AND METHODS). We found that the F-score is near 1.0 in segmenting Brp::rGFP clusters within DPM and APL neurons and achieved > 0.90 in KCs with certain combinations of segmentation parameters (Fig. 2B).

To confirm that Brp clusters represent AZs, we quantified the number of Brp::rGFP clusters in DPM and APL neurons specifically and compared it to the connectome data. We found that cluster counts closely matched the number of AZs annotated by the hemibrain connectome (Fig. 2C) (*10*). This result validated our method that accurately isolated Brp::rGFP clusters corresponding to single AZs.

AZ profiles within KCs are compartmentally heterogeneous

Brp accumulation at individual AZs is known to be heterogeneous even within a single motor neuron (*1–3*, *32*). To study such AZ heterogeneity in CNS neurons, we quantified the signal intensity of individual Brp::rGFP clusters in MB lobes. Using KC subtype-specific drivers to direct split-GFP reconstitution in γ KC (MB009B-GAL4), α'/β' KCs (MB370B-GAL4) and α/β KCs (MB008B-GAL4). we found that Brp::rGFP intensities are highly diverse in all KC subtypes (Fig. 3A).

To visualize spatial patterns of Brp::rGFP intensity in each KC subtype, we reconstructed the 3D distribution of Brp::rGFP clusters and color-coded them by signal intensities (Fig. 3B). We found that clusters showed noticeable intensity differences between compartments in all subtypes. Adjacent compartments such as γ1 and γ2, β'2 and β'1, α2 and α3, showed drastic differences (Fig. 3B). These compartmental patterns were stable across individuals (*33*) . This result suggests that AZs in different compartments have distinct structures. Since individual KCs of each subtype synapse onto all compartments (*9–11*, *34*), this Brp compartmental heterogeneity is likely formed intracellularly.

Intracellular heterogeneity of Brp density and cell-type dependent diversity

Super-resolution microscopy has shown that the Brp molecular density at individual AZs is dynamically adjusted in motor neurons (*35*, *36*). We hypothesized that the amount of Brp does not necessarily correlate with AZ cluster size. To verify this, we quantified both the volume (number of voxels within a 3D ROI) and the Brp::rGFP intensity of each cluster. We found clusters with similar sizes exhibit different signal intensities, suggesting the heterogeneity of Brp density at individual AZs (Fig. 4A). Correlation analysis between the Brp::rGFP intensity and cluster volume revealed a substantial variability among cell types. Specifically, the correlation is high in KCs with a significant difference among KC subtypes. In contrast, the correlation is low for DPM and APL neurons (Fig. 4B-E). These results suggest a cell-type dependent variability of the Brp density of individual clusters.

Stereotypy of AZ spatial distribution at single-cell level

To study the individual variability in AZ distribution, we focused on single neurons innervating the MB. MB504B-GAL4 labels four types of single PPL1 DANs projecting to distinct compartments (*37*). Using this driver, we analyzed the Brp::rGFP distribution in each compartment and found it uneven in both α2α'2 and α3 (Fig. 6A-B). To better characterize the cluster distribution, we calculated the "AZ density" defined as the number of Brp::rGFP clusters surrounding a particular cluster within a specified radius (see Fig. 2A and MATERIALS AND METHODS for detail). By color-coding Brp::rGFP clusters according to their AZ density, we found that AZ were more localized to the core of α3. This pattern is consistent across individuals (Fig. 6C-D), suggesting a stereotyped AZ distribution within PPL1-α3 neurons.

We extended the analysis to two other single pairs of neurons innervating the MBs, the DPM and APL neurons. Visualizing AZ density revealed a stereotyped and compartment specific distribution in DPM neurons (Fig. 5A). Specifically, the AZ density was

constantly high in the α'/β' lobes across all individuals, consistent with the known functional importance of DPM branches in the α'/β' lobes (*28*). In contrast, this compartmental pattern is less pronounced in APL. Notably, the ratio of AZ density between α3 and α'3 is strikingly different among individuals (Fig. 5B). Taken together, these data suggest that the individual variability in AZ distribution depends on the cell type.

Local regulation of AZ structures

We have found the compartmentalized Brp distributions in KCs. Although, highly variable Brp::rGFP intensities among nearby clusters hinder further pattern analysis (Fig. 3B). To reduce such high frequency noises, we calculated the "local intensity" for each cluster (the average Brp::rGFP intensity of all surrounding clusters within a specified radius *r*, see MATERIALS AND METHODS for detail). By analyzing the local intensity in γ KCs, we further identified AZ "hot spots", sub-compartment-sized small patches with high local intensities, on top of the compartmental differences (Fig. 7A). Since Brp tend to localize to AZ-dense boutons in motor neurons (*2*), we hypothesized that these hot spots correspond to regions with higher AZ densities. Indeed, we found that hot spots appear in high AZ densities regions and the correlation between the local intensity and the AZ density is high in KCs (Fig. 7A, 7C). In contrast, for DPM and APL neurons, we observed patches of high local intensities while they are not associated with high AZ density regions (Fig. 7B-C).

We further examined potential local patterns among AZs in proximity by calculating the correlation of Brp::rGFP intensities between nearest neighbor clusters. This analysis revealed strong correlations in KCs but not in DPM (Fig. 7D). These results suggest previously unnoticed sub-compartmental synaptic structures organized across individual KCs. Such local structures may play an important role in the function of KCs, such as in associative learning. Given that Rutabaga (Rut), a calcium/calmodulin-dependent adenylyl cyclase, is required in KCs for associative learnings (*38*), we knocked-down Rut in KCs using RNA interference (*39*) (RNAi). Following Rut knock-down, the location of high local intensity patches was largely disrupted (Fig. 8A). Furthermore, we found both the local intensity-AZ density correlation and the nearest neighbor correlation were significantly reduced (Fig. 8B-C). Altogether, we propose that cAMP signaling regulates the local AZ structures, supporting the synaptic function of KCs.

Discussion

Leveraging the CRISPR/Cas9 genome editing and split-GFP technique, we systematically profiled presynaptic structures of MB neurons in a cell-type-specific manner. This approach enabled high-throughput analysis of multiple brain samples and the detailed characterizations revealing previously inaccessible AZ structural features of CNS neurons.

Single-cell level analysis of AZ profiles revealed the cell-type-specific stereotypy in AZ spatial regulation (Fig. 5-6). We found that the AZ density in DPM neurons is consistently high in the α'/β' lobes across individuals (Fig. 6). Previous studies demonstrated that overexpression of the DScam variant in DPM neurons did not disrupt α'/β' lobe innervation and appetitive memory formation (*28*). The observed AZ distribution stereotypy of DPM explains the functional significance of DPM innervation on the α'/β' lobes. In PPL1-α3 DAN, we identified a stereotyped AZ distribution presented within the α3 compartment (Fig. 5). This localized pattern contrasts with the broader AZ organization observed in DPM and may underlie the functional difference between KC

subtypes in associative learning (*40*). While the AZ distribution stereotypy of APL is less pronounced, we found strong correlations between Brp::rGFP intensities of neighboring AZs compared to DPM. This suggests that AZs in APL neurons are optimized for highly local environments, consistent with APL's role in providing localized inhibitions to KC synapses (*41*). Collectively, the spatial scale of AZ organizations aligns with the function of individual CNS neurons.

We observed that Brp::rGFP intensity correlates strongly to AZ size in KC subtypes, in contrast to DPM and APL neurons (Fig. 4). Previous studies using localization microscopy showed that the molecular density of AZ proteins can be dynamically adjusted in motor neurons, potentially modulating the presynaptic release (*35*, *36*, *42*). The variable ratio between Brp::rGFP intensity and AZ size in DPM and APL neurons may represent AZs with distinct Brp molecular densities and therefore different functional modes. Notably, a recent study successfully predicted the neurotransmitter type of neurons using the ultrastructure of dense projections as one of the parameters (*43*), suggesting neurotransmitter-specific AZ structures. Given that both DPM and APL neurons are suggested to release multiple neurotransmitters (*25*, *29*, *44–48*), AZs with distinct Brp densities might be optimized for releasing different types of neurotransmitters.

In KCs, spatial analysis revealed AZ "hot spots", regions with high Brp localization and AZ densities. Additionally, we found strong correlations between Brp::rGFP intensities at neighboring AZs within KCs (Fig. 7). These results suggest previously unidentified, highly localized sub-compartmental AZ structures. Individual presynaptic boutons of KCs have highly heterogeneous plasticity upon the dopamine modulation and associative learning (*49*, *50*). The cause and function of such individuality remain elusive. A recent study found sub-compartmentally heterogeneous activities of dopamine terminals, which plausibly associate with memory specificity (*51*). Heterogenous dopamine modulations may therefore group and differentiate local AZ subsets formed across individual KCs. Moreover, cAMP signaling plays a crucial role in the AZ structural plasticity, especially during associative memory formation (*33*, *42*, *52*). Consistently, we found that knocking-down Rut, a calcium/calmodulin dependent adenylyl cyclase that is essential for associative memory formation (*38*), disrupted sub-compartmental organizations of AZs (Fig. 8). Taken together, sub-compartmental AZ structures may support associative memory formation through localized remodeling (*18*, *19*).

Materials and Methods

Fly strains

Flies were maintained on standard cornmeal food at 25 °C under a 12:12 h light-dark cycle for all experiments. All flies used for experiments are 3-7 days old adult males. Flies were transferred to fresh food vials after hatching and flipped every two days before experiments. The GAL4-UAS system was used to express transgenes, and balancers were removed for animals used in all experiments. Fly strains and resources used in this study are as follow: MB008B-GAL4 (BDSC_68291); MB009B-GAL4 (BDSC_68292); MB370B-GAL4 (BDSC_68319); MB504B-GAL4 (BDSC_68329) (*22*) ; VT64246-GAL4 (VDRC 204311) (*53*); GH146-GAL4 (BDSC_30026, by Dr. Liqun Luo); R58E02-GAL4 (BDSC_41347); R13F02-GAL4 (BDSC_48571) (*54*) ; UAS-CD4::tdTomato (BDSC_35841, by Dr. Yhu Nung Jan & Chun Han); UAS-Rut-RNAi (BDSC_80468) (*55*) ; *brp::GFP11* (*33*) ; UAS-GFP1-10 (*56*).

Imaging sample preparation

Animals used in experiments involving comparisons between control and experimental groups were dissected on the same day. Data were collected from multiple batches of experiments performed on different days. Flies were anesthetized by ice and placed on ice before dissection. The dissection was performed in cold PBS to collect the brain without the ventral nerve cord. The brains were subsequently fixed by 2% paraformaldehyde for 1 h and then washed 3×20 min by 0.1% PBT (0.1% Triton X-100 in PBS) in a PCR tube, typically 5-6 brains in one tube. Samples were mounted on microscope slides using mounting medium SeeDB2S (*57*).

Confocal microscopy image acquisition

The image acquisition was performed using an Olympus FV1200 confocal microscope platform equipped with both PMT and GaAsP high sensitivity detectors and a 60×/1.42 NA oil immersion objective (PLAPON60XO, Olympus). The Kalman filter was turned on to 2× averaging while scanning. For Brp::rGFP samples in all GAL4 types, scanning speed: 2 µs/pixel with a voxel size of lateral 0.079 × 0.079 × axial 0.370 µm. For experimental point spread function (PSF) imaging, SeeDB2S immersed beads were scanned in a setting that is 60×/1.42 NA oil immersion objective; 473 nm laser power: 2.0%; 559 nm laser power: 1.5%; voxel size: 0.079 µm × 0.079 µm × 0.370 µm; scanning speed: 4 µs/pixel, to produce multiple bead images.

PSF acquisition and image deconvolution

Sub-resolution fluorescent beads (Tetraspeck Microspheres 0.1 µm, Thermo Fisher Scientific, T7279) were imaged to generate the PSF. The bead solution was diluted with distilled water and sonicated several times to eliminate aggregation. PSF images acquired were processed using Amira software (Thermo Fisher Scientific) with the Extract Point Spread Function module. The PSFs extracted from each image were averaged to create a single PSF for later image deconvolution (Resizing voxel size: 0.079 µm × 0.079 µm × 0.370 µm; 32 pixels × 32 pixels × 21 slices of image size). Image deconvolution was performed by using the Richardson-Lucy iterative non-blind algorithm in a Fiji plugin DeconvolutionLab2 (*58*), or by CLIJ2 GPU-based Richardson-Lucy deconvolution (*59*). Images were deconvolved 20 times iteratively to improve image quality.

Brp clusters segmentation and data analysis

For Brp::rGFP cluster detection, the image stack size was adjusted to double the XY plate pixel number using Fiji to increase the detection precision. The images were subsequently processed using the 3D maxima finder and the 3D spot segmentation function of the 3D suite package in Fiji. 3D maxima were identified for each cluster and used as the starting point for pixel clustering (*31*). An intensity threshold (threshold) and the noise tolerance were set to reduce noise and adjust the sensitivity of 3D maxima detection respectively. The threshold set the value of all pixels that have values below the threshold to NaN (not a number). The noise tolerance is set in the 3D maxima finder. To be noticed, the threshold is only applied to the image used to find 3D maxima. The 3D maxima finder generates the 3D maxima. The 3D segmentation function then requires the 3D maxima and the raw image, so that there is no intensity cut affecting the measurement of cluster volume (used deconvolved image). The local thresholding method for the 3D segmentation was set to Gaussian fit, with the "SD value" set to 2. Cluster volume was measured as the voxel count within the 3D ROI.

The above procedures may include a tiling and stitching step for images and data because of the limited computer power. Typically, an image was tiled into 25 sub-stacks with overlapped margins. After being processed separately, the data acquired from all tiled sub-

stacks was stitched back with a deletion of overlapping data points to generate the complete detection result. Nearest neighbors were identified for each punctum and spatial distances in between were calculated using Python. For each sample, mean NND was calculated separately. For a particular Brp::rGFP cluster, the number of surrounding clusters within r ($r = 3 \times$ mean NND) spherically including itself is referred as the "AZ density". The "local intensity" of a particular Brp::rGFP cluster is the average of Brp::rGFP intensity of all clusters surrounding within r ($r = 3 \times$ mean NND) including itself. The plot function of Python was used to plot the color-coded 3D reconstructed maps.

F-score calculation

The 3D detection parameters were optimized by comparing the 3D maxima detection results to manually defined ground truths. The F-score was used to assess detection precision. F-score is the harmonic mean of a system's precision and recall value, calculated by the following formula: 2 × [(Precision × Recall) / (Precision + Recall)]. The precision is the number of true positives divided by the total number of identified positives, including incorrect identification. The recall is the number of true positives divided by the total number of true data points defined as the ground truth. F-scores shown in Fig. 1 were automatically calculated using a customized Fiji Marco that aligned 3D maxima with ground truth. Different combinations of noise threshold and noise tolerance were tested for the test images cropped from raw images.

Statistical analysis

Statistical analysis was performed using GraphPad Prism version 8, 9 and 10 or Python. For statistical comparisons, Kruskal-Wallis test with original False Discovery Rate method of Benjamini and Hochberg correction was applied. A desired false discovery rate of 0.05. Pearson's correlation coefficient (R) was calculated using Python.

References

1. N. Ehmann, S. van de Linde, A. Alon, D. Ljaschenko, X. Z. Keung, T. Holm, A. Rings, A. DiAntonio, S. Hallermann, U. Ashery, M. Heckmann, M. Sauer, R. J. Kittel, Quantitative super-resolution imaging of Bruchpilot distinguishes active zone states. *Nat Commun* **5**, 4650 (2014).
2. M. M. Paul, M. Pauli, N. Ehmann, S. Hallermann, M. Sauer, R. J. Kittel, M. Heckmann, Bruchpilot and Synaptotagmin collaborate to drive rapid glutamate release and active zone differentiation. *Front Cell Neurosci* **9**, 29 (2015).
3. Y. Akbergenova, K. L. Cunningham, Y. V. Zhang, S. Weiss, J. T. Littleton, Characterization of developmental and molecular factors underlying release heterogeneity at Drosophila synapses. *Elife* **7**, e38268 (2018).
4. Z. L. Newman, D. Bakshinskaya, R. Schultz, S. J. Kenny, S. Moon, K. Aghi, C. Stanley, N. Marnani, R. Li, J. Bleier, K. Xu, E. Y. Isacoff, Determinants of synapse diversity revealed by super-resolution quantal transmission and active zone imaging. *Nat Commun* **13**, 229 (2022).
5. R. J. Kittel, C. Wichmann, T. M. Rasse, W. Fouquet, M. Schmidt, A. Schmid, D. A. Wagh, C. Pawlu, R. R. Kellner, K. I. Willig, S. W. Hell, E. Buchner, M. Heckmann, S. J. Sigrist, Bruchpilot Promotes Active Zone Assembly, Ca^{2+} Channel Clustering, and Vesicle Release. *Science* **312**, 1051–1054 (2006).
6. D. A. Wagh, T. M. Rasse, E. Asan, A. Hofbauer, I. Schwenkert, H. Dürrbeck, S. Buchner, M.-C. Dabauvalle, M. Schmidt, G. Qin, C. Wichmann, R. Kittel, S. J. Sigrist, E.

Buchner, Bruchpilot, a Protein with Homology to ELKS/CAST, Is Required for Structural Integrity and Function of Synaptic Active Zones in Drosophila. *Neuron* **49**, 833–844 (2006).
7. W. Fouquet, D. Owald, C. Wichmann, S. Mertel, H. Depner, M. Dyba, S. Hallermann, R. J. Kittel, S. Eimer, S. J. Sigrist, Maturation of active zone assembly by Drosophila Bruchpilot. *J Cell Biol* **186**, 129–145 (2009).
8. T. Matkovic, M. Siebert, E. Knoche, H. Depner, S. Mertel, D. Owald, M. Schmidt, U. Thomas, A. Sickmann, D. Kamin, S. W. Hell, J. Bürger, C. Hollmann, T. Mielke, C. Wichmann, S. J. Sigrist, The Bruchpilot cytomatrix determines the size of the readily releasable pool of synaptic vesicles. *J Cell Biol* **202**, 667–683 (2013).
9. Z. Zheng, J. S. Lauritzen, E. Perlman, C. G. Robinson, M. Nichols, D. Milkie, O. Torrens, J. Price, C. B. Fisher, N. Sharifi, S. A. Calle-Schuler, L. Kmecova, I. J. Ali, B. Karsh, E. T. Trautman, J. A. Bogovic, P. Hanslovsky, G. S. X. E. Jefferis, M. Kazhdan, K. Khairy, S. Saalfeld, R. D. Fetter, D. D. Bock, A Complete Electron Microscopy Volume of the Brain of Adult Drosophila melanogaster. *Cell* **174**, 730-743.e22 (2018).
10. L. K. Scheffer, C. S. Xu, M. Januszewski, Z. Lu, S. Takemura, K. J. Hayworth, G. B. Huang, K. Shinomiya, J. Maitlin-Shepard, S. Berg, J. Clements, P. M. Hubbard, W. T. Katz, L. Umayam, T. Zhao, D. Ackerman, T. Blakely, J. Bogovic, T. Dolafi, D. Kainmueller, T. Kawase, K. A. Khairy, L. Leavitt, P. H. Li, L. Lindsey, N. Neubarth, D. J. Olbris, H. Otsuna, E. T. Trautman, M. Ito, A. S. Bates, J. Goldammer, T. Wolff, R. Svirskas, P. Schlegel, E. Neace, C. J. Knecht, C. X. Alvarado, D. A. Bailey, S. Ballinger, J. A. Borycz, B. S. Canino, N. Cheatham, M. Cook, M. Dreher, O. Duclos, B. Eubanks, K. Fairbanks, S. Finley, N. Forknall, A. Francis, G. P. Hopkins, E. M. Joyce, S. Kim, N. A. Kirk, J. Kovalyak, S. A. Lauchie, A. Lohff, C. Maldonado, E. A. Manley, S. McLin, C. Mooney, M. Ndama, O. Ogundeyi, N. Okeoma, C. Ordish, N. Padilla, C. M. Patrick, T. Paterson, E. E. Phillips, E. M. Phillips, N. Rampally, C. Ribeiro, M. K. Robertson, J. T. Rymer, S. M. Ryan, M. Sammons, A. K. Scott, A. L. Scott, A. Shinomiya, C. Smith, K. Smith, N. L. Smith, M. A. Sobeski, A. Suleiman, J. Swift, S. Takemura, I. Talebi, D. Tarnogorska, E. Tenshaw, T. Tokhi, J. J. Walsh, T. Yang, J. A. Horne, F. Li, R. Parekh, P. K. Rivlin, V. Jayaraman, M. Costa, G. S. Jefferis, K. Ito, S. Saalfeld, R. George, I. A. Meinertzhagen, G. M. Rubin, H. F. Hess, V. Jain, S. M. Plaza, A connectome and analysis of the adult Drosophila central brain. *Elife* **9**, e57443 (2020).
11. S. Takemura, K. J. Hayworth, G. B. Huang, M. Januszewski, Z. Lu, E. C. Marin, S. Preibisch, C. S. Xu, J. Bogovic, A. S. Champion, H. S. Cheong, M. Costa, K. Eichler, W. Katz, C. Knecht, F. Li, B. J. Morris, C. Ordish, P. K. Rivlin, P. Schlegel, K. Shinomiya, T. Stürner, T. Zhao, G. Badalamente, D. Bailey, P. Brooks, B. S. Canino, J. Clements, M. Cook, O. Duclos, C. R. Dunne, K. Fairbanks, S. Fang, S. Finley-May, A. Francis, R. George, M. Gkantia, K. Harrington, G. P. Hopkins, J. Hsu, P. M. Hubbard, A. Javier, D. Kainmueller, W. Korff, J. Kovalyak, D. Krzemiński, S. A. Lauchie, A. Lohff, C. Maldonado, E. A. Manley, C. Mooney, E. Neace, M. Nichols, O. Ogundeyi, N. Okeoma, T. Paterson, E. Phillips, E. M. Phillips, C. Ribeiro, S. M. Ryan, J. T. Rymer, A. K. Scott, A. L. Scott, D. Shepherd, A. Shinomiya, C. Smith, N. Smith, A. Suleiman, S. Takemura, I. Talebi, I. F. Tamimi, E. T. Trautman, L. Umayam, J. J. Walsh, T. Yang, G. M. Rubin, L. K. Scheffer, J. Funke, S. Saalfeld, H. F. Hess, S. M. Plaza, G. M. Card, G. S. Jefferis, S. Berg, A Connectome of the Male Drosophila Ventral Nerve Cord. doi: 10.7554/elife.97769.1 (2024).
12. P. Schlegel, Y. Yin, A. S. Bates, S. Dorkenwald, K. Eichler, P. Brooks, D. S. Han, M. Gkantia, M. dos Santos, E. J. Munnelly, G. Badalamente, L. S. Capdevila, V. A. Sane, A. M. C. Fragniere, L. Kiassat, M. W. Pleijzier, T. Stürner, I. F. M. Tamimi, C. R. Dunne, I. Salgarella, A. Javier, S. Fang, E. Perlman, T. Kazimiers, S. R. Jagannathan, A. Matsliah,

A. R. Sterling, S. Yu, C. E. McKellar, P. Schlegel, Y. Yin, S. Dorkenwald, K. Eichler, P. Brooks, M. Gkantia, G. Badalamente, L. S. Capdevila, I. F. M. Tamimi, I. Salgarella, A. Javier, S. Fang, E. Perlman, A. Matsliah, S. Yu, C. E. McKellar, K. Kruk, D. Bland, Z. Lenizo, A. T. Burke, K. P. Willie, A. S. Bates, N. Serafetinidis, N. Hadjerol, R. Willie, B. Silverman, J. A. Ocho, J. Bañez, R. A. Candilada, J. Gager, A. Kristiansen, N. Panes, A. Yadav, R. Tancontian, S. Serona, J. I. Dolorosa, K. J. Vinson, D. Garner, R. Salem, A. Dagohoy, J. Skelton, M. Lopez, T. Stocks, A. Pandey, D. J. Akiatan, J. Hebditch, C. David, D. Sapkal, S. M. Monungolh, V. Sane, M. L. Pielago, M. Albero, J. Laude, M. dos Santos, D. Deutsch, Z. Vohra, K. Wang, A. M. Gogo, E. Kind, A. J. Mandahay, C. Martinez, J. D. Asis, C. Nair, D. Patel, M. Manaytay, C. A. Lim, P. L. Ampo, M. D. Pantujan, D. Bautista, R. Rana, J. Seguido, B. Parmar, J. C. Saguimpa, M. Moore, M. W. Pleijzier, M. Larson, J. Hsu, I. Joshi, D. Kakadiya, A. Braun, C. Pilapil, K. Parmar, Q. Vanderbeck, C. Dunne, E. Munnelly, C. H. Kang, L. Lörsch, J. Lee, L. Kmecova, G. Sancer, C. Baker, J. Joroff, S. Calle, Y. Patel, O. Sato, J. Salocot, F. Salman, S. Molina-Obando, M. Bui, M. Lichtenberger, E. Tamboboy, K. Molloy, A. E. Santana-Cruz, A. Hernandez, S. Yu, M. Sorek, A. Diwan, M. Patel, T. R. Aiken, S. Morejohn, S. Koskela, T. Yang, D. Lehmann, J. Chojetzki, S. Sisodiya, S. Koolman, P. K. Shiu, S. Cho, A. Bast, B. Reicher, M. Blanquart, L. Houghton, H. Choi, M. Ioannidou, M. Collie, J. Eckhardt, B. Gorko, L. Guo, Z. Zheng, A. Poh, M. Lin, I. Taisz, W. Murfin, Á. S. Díez, N. Reinhard, P. Gibb, N. Patel, S. Kumar, M. Yun, M. Wang, D. Jones, L. Encarnacion-Rivera, A. Oswald, A. Jadia, M. Erginkaya, N. Drummond, L. Walter, I. Tastekin, X. Zhong, Y. Mabuchi, F. J. F. Santiago, U. Verma, N. Byrne, E. Kunze, T. Crahan, R. Margossian, H. Kim, I. Georgiev, F. Szorenyi, A. Adachi, B. Bargeron, T. Stürner, D. Demarest, B. Gür, A. N. Becker, R. Turnbull, A. Morren, A. Sandoval, A. Moreno-Sanchez, D. A. Pacheco, E. Samara, H. Croke, A. Thomson, C. Laughland, S. B. Dutta, P. G. A. de Antón, B. Huang, P. Pujols, I. Haber, A. González-Segarra, A. Lin, D. T. Choe, V. Lukyanova, N. Mancini, Z. Liu, T. Okubo, M. A. Flynn, G. Vitelli, M. Laturney, F. Li, S. Cao, C. Manyari-Diaz, H. Yim, A. D. Le, K. Maier, S. Yu, Y. Nam, D. Bąba, A. Abusaif, A. Francis, J. Gayk, S. S. Huntress, R. Barajas, M. Kim, X. Cui, A. R. Sterling, G. R. Sterne, A. Li, K. Park, G. Dempsey, A. Mathew, J. Kim, T. Kim, G. Wu, S. Dhawan, M. Brotas, C. Zhang, S. Bailey, A. D. Toro, K. Lee, T. Macrina, C. Schneider-Mizell, S. Popovych, O. Ogedengbe, R. Yang, A. Halageri, W. Silversmith, S. Gerhard, A. Champion, N. Eckstein, D. Ih, N. Kemnitz, M. Castro, Z. Jia, J. Wu, E. Mitchell, B. Nehoran, S. Mu, J. A. Bae, R. Lu, R. Morey, K. Kuehner, D. Brittain, C. S. Jordan, D. J. Anderson, R. Behnia, S. S. Bidaye, A. Borst, E. Chiappe, F. Collman, K. J. Colodner, A. Dacks, B. Dickson, J. Funke, D. Garcia, S. Hampel, V. Hartenstein, B. Hassan, C. Helfrich-Forster, W. Huetteroth, J. Kim, S. S. Kim, Y.-J. Kim, J. Y. Kwon, W.-C. Lee, G. A. Linneweber, G. Maimon, R. Mann, S. Noselli, M. Pankratz, L. Prieto-Godino, J. Read, M. Reiser, K. von Reyn, C. Ribeiro, K. Scott, A. M. Seeds, M. Selcho, M. Silies, J. Simpson, S. Waddell, M. F. Wernet, R. I. Wilson, F. W. Wolf, Z. Yao, N. Yapici, M. Zandawala, M. Costa, H. S. Seung, M. Murthy, D. D. Bock, G. S. X. E. Jefferis, M. Costa, H. S. Seung, M. Murthy, V. Hartenstein, D. D. Bock, G. S. X. E. Jefferis, Whole-brain annotation and multi-connectome cell typing of Drosophila. *Nature* **634**, 139–152 (2024).

13. S. Dorkenwald, A. Matsliah, A. R. Sterling, P. Schlegel, S. Yu, C. E. McKellar, A. Lin, M. Costa, K. Eichler, Y. Yin, W. Silversmith, C. Schneider-Mizell, C. S. Jordan, D. Brittain, A. Halageri, K. Kuehner, O. Ogedengbe, R. Morey, J. Gager, K. Kruk, E. Perlman, R. Yang, D. Deutsch, D. Bland, M. Sorek, R. Lu, T. Macrina, K. Lee, J. A. Bae, S. Mu, B. Nehoran, E. Mitchell, S. Popovych, J. Wu, Z. Jia, M. A. Castro, N. Kemnitz, D. Ih, A. S. Bates, N. Eckstein, J. Funke, F. Collman, D. D. Bock, G. S. X. E. Jefferis, H. S. Seung, M. Murthy, S. Dorkenwald, A. Matsliah, A. R. Sterling, P. Schlegel, S. Yu, C. E.

McKellar, A. Lin, M. Costa, K. Eichler, Y. Yin, W. Silversmith, C. Schneider-Mizell, C. S. Jordan, D. Brittain, A. Halageri, K. Kuehner, O. Ogedengbe, R. Morey, J. Gager, K. Kruk, E. Perlman, D. Deutsch, D. Bland, M. Sorek, R. Lu, T. Macrina, K. Lee, J. A. Bae, S. Mu, B. Nehoran, E. Mitchell, S. Popovych, J. Wu, Z. Jia, M. A. Castro, N. Kemnitz, D. Ih, A. S. Bates, N. Eckstein, J. Funke, F. Collman, D. D. Bock, G. S. X. E. Jefferis, H. S. Seung, M. Murthy, Z. Lenizo, A. T. Burke, K. P. Willie, N. Serafetinidis, N. Hadjerol, R. Willie, B. Silverman, J. A. Ocho, J. Bañez, R. A. Candilada, A. Kristiansen, N. Panes, A. Yadav, R. Tancontian, S. Serona, J. I. Dolorosa, K. J. Vinson, D. Garner, R. Salem, A. Dagohoy, J. Skelton, M. Lopez, L. S. Capdevila, G. Badalamente, T. Stocks, A. Pandey, D. J. Akiatan, J. Hebditch, C. David, D. Sapkal, S. M. Monungolh, V. Sane, M. L. Pielago, M. Albero, J. Laude, M. dos Santos, Z. Vohra, K. Wang, A. M. Gogo, E. Kind, A. J. Mandahay, C. Martinez, J. D. Asis, C. Nair, D. Patel, M. Manaytay, I. F. M. Tamimi, C. A. Lim, P. L. Ampo, M. D. Pantujan, A. Javier, D. Bautista, R. Rana, J. Seguido, B. Parmar, J. C. Saguimpa, M. Moore, M. W. Pleijzier, M. Larson, J. Hsu, I. Joshi, D. Kakadiya, A. Braun, C. Pilapil, M. Gkantia, K. Parmar, Q. Vanderbeck, I. Salgarella, C. Dunne, E. Munnelly, C. H. Kang, L. Lörsch, J. Lee, L. Kmecova, G. Sancer, C. Baker, J. Joroff, S. Calle, Y. Patel, O. Sato, S. Fang, J. Salocot, F. Salman, S. Molina-Obando, P. Brooks, M. Bui, M. Lichtenberger, E. Tamboboy, K. Molloy, A. E. Santana-Cruz, A. Hernandez, S. Yu, A. Diwan, M. Patel, T. R. Aiken, S. Morejohn, S. Koskela, T. Yang, D. Lehmann, J. Chojetzki, S. Sisodiya, S. Koolman, P. K. Shiu, S. Cho, A. Bast, B. Reicher, M. Blanquart, L. Houghton, H. Choi, M. Ioannidou, M. Collie, J. Eckhardt, B. Gorko, L. Guo, Z. Zheng, A. Poh, M. Lin, I. Taisz, W. Murfin, Á. S. Díez, N. Reinhard, P. Gibb, N. Patel, S. Kumar, M. Yun, M. Wang, D. Jones, L. Encarnacion-Rivera, A. Oswald, A. Jadia, M. Erginkaya, N. Drummond, L. Walter, I. Tastekin, X. Zhong, Y. Mabuchi, F. J. F. Santiago, U. Verma, N. Byrne, E. Kunze, T. Crahan, R. Margossian, H. Kim, I. Georgiev, F. Szorenyi, A. Adachi, B. Bargeron, T. Stürner, D. Demarest, B. Gür, A. N. Becker, R. Turnbull, A. Morren, A. Sandoval, A. Moreno-Sanchez, D. A. Pacheco, E. Samara, H. Croke, A. Thomson, C. Laughland, S. B. Dutta, P. G. A. de Antón, B. Huang, P. Pujols, I. Haber, A. González-Segarra, D. T. Choe, V. Lukyanova, N. Mancini, Z. Liu, T. Okubo, M. A. Flynn, G. Vitelli, M. Laturney, F. Li, S. Cao, C. Manyari-Diaz, H. Yim, A. D. Le, K. Maier, S. Yu, Y. Nam, D. Bąba, A. Abusaif, A. Francis, J. Gayk, S. S. Huntress, R. Barajas, M. Kim, X. Cui, G. R. Sterne, A. Li, K. Park, G. Dempsey, A. Mathew, J. Kim, T. Kim, G. Wu, S. Dhawan, M. Brotas, C. Zhang, S. Bailey, A. D. Toro, R. Yang, S. Gerhard, A. Champion, D. J. Anderson, R. Behnia, S. S. Bidaye, A. Borst, E. Chiappe, K. J. Colodner, A. Dacks, B. Dickson, D. Garcia, S. Hampel, V. Hartenstein, B. Hassan, C. Helfrich-Forster, W. Huetteroth, J. Kim, S. S. Kim, Y.-J. Kim, J. Y. Kwon, W.-C. Lee, G. A. Linneweber, G. Maimon, R. Mann, S. Noselli, M. Pankratz, L. Prieto-Godino, J. Read, M. Reiser, K. von Reyn, C. Ribeiro, K. Scott, A. M. Seeds, M. Selcho, M. Silies, J. Simpson, S. Waddell, M. F. Wernet, R. I. Wilson, F. W. Wolf, Z. Yao, N. Yapici, M. Zandawala, Neuronal wiring diagram of an adult brain. *Nature* **634**, 124–138 (2024).

14. S. Sachse, E. Rueckert, A. Keller, R. Okada, N. K. Tanaka, K. Ito, L. B. Vosshall, Activity-Dependent Plasticity in an Olfactory Circuit. *Neuron* **56**, 838–850 (2007).

15. G. F. Gilestro, G. Tononi, C. Cirelli, Widespread Changes in Synaptic Markers as a Function of Sleep and Wakefulness in Drosophila. *Science* **324**, 109–112 (2009).

16. M. P. Fernández, J. Berni, M. F. Ceriani, Circadian Remodeling of Neuronal Circuits Involved in Rhythmic Behavior. *PLoS Biol.* **6**, e69 (2008).

17. M. C. Kremer, F. Christiansen, F. Leiss, M. Paehler, S. Knapek, T. F. M. Andlauer, F. Förstner, P. Kloppenburg, S. J. Sigrist, G. Tavosanis, Structural Long-Term Changes at Mushroom Body Input Synapses. *Curr Biol* **20**, 1938–1944 (2010).

18. O. Turrel, N. Ramesh, M. J. F. Escher, A. Pooryasin, S. J. Sigrist, Transient active zone remodeling in the Drosophila mushroom body supports memory. *Curr Biol*, doi: 10.1016/j.cub.2022.10.017 (2022).
19. X. Zhang, Q. Li, L. Wang, Z.-J. Liu, Y. Zhong, Active Protection: Learning-Activated Raf/MAPK Activity Protects Labile Memory from Rac1-Independent Forgetting. *Neuron* **98**, 142-155.e4 (2018).
20. Y. Chen, O. Akin, A. Nern, C. Y. K. Tsui, M. Y. Pecot, S. L. Zipursky, Cell-type-Specific Labeling of Synapses In Vivo through Synaptic Tagging with Recombination. *Neuron* **81**, 280–293 (2014).
21. R. L. Davis, Learning and memory using Drosophila melanogaster : a focus on advances made in the fifth decade of research. *GENETICS*, doi: 10.1093/genetics/iyad085 (2023).
22. Y. Aso, D. Hattori, Y. Yu, R. M. Johnston, N. A. Iyer, T.-T. Ngo, H. Dionne, L. Abbott, R. Axel, H. Tanimoto, G. M. Rubin, The neuronal architecture of the mushroom body provides a logic for associative learning. *Elife* **3**, e04577 (2014).
23. J. L. Pitman, W. Huetteroth, C. J. Burke, M. J. Krashes, S.-L. Lai, T. Lee, S. Waddell, A Pair of Inhibitory Neurons Are Required to Sustain Labile Memory in the Drosophila Mushroom Body. *Curr Biol* **21**, 855–861 (2011).
24. A. C. Lin, A. M. Bygrave, A. de Calignon, T. Lee, G. Miesenböck, Sparse, decorrelated odor coding in the mushroom body enhances learned odor discrimination. *Nat Neurosci* **17**, 559–568 (2014).
25. X. Liu, R. L. Davis, The GABAergic anterior paired lateral neuron suppresses and is suppressed by olfactory learning. *Nat. Neurosci.* **12**, 53–59 (2009).
26. D. Yu, A. C. Keene, A. Srivatsan, S. Waddell, R. L. Davis, Drosophila DPM Neurons Form a Delayed and Branch-Specific Memory Trace after Olfactory Classical Conditioning. *Cell* **123**, 945–957 (2005).
27. A. C. Keene, M. Stratmann, A. Keller, P. N. Perrat, L. B. Vosshall, S. Waddell, Diverse Odor-Conditioned Memories Require Uniquely Timed Dorsal Paired Medial Neuron Output. *Neuron* **44**, 521–533 (2004).
28. A. C. Keene, M. J. Krashes, B. Leung, J. A. Bernard, S. Waddell, Drosophila Dorsal Paired Medial Neurons Provide a General Mechanism for Memory Consolidation. *Curr Biol* **16**, 1524–1530 (2006).
29. P. R. Haynes, B. L. Christmann, L. C. Griffith, A single pair of neurons links sleep to memory consolidation in Drosophila melanogaster. *eLife* **4**, e03868 (2015).
30. S. Waddell, J. D. Armstrong, T. Kitamoto, K. Kaiser, W. G. Quinn, The amnesiac Gene Product Is Expressed in Two Neurons in the Drosophila Brain that Are Critical for Memory. *Cell* **103**, 805–813 (2000).
31. J. Ollion, J. Cochennec, F. Loll, C. Escudé, T. Boudier, TANGO: a generic tool for high-throughput 3D image analysis for studying nuclear organization. *Bioinformatics* **29**, 1840–1841 (2013).
32. S. J. Gratz, P. Goel, J. J. Bruckner, R. X. Hernandez, K. Khateeb, G. T. Macleod, D. Dickman, K. M. O'Connor-Giles, Endogenous tagging reveals differential regulation of Ca2+ channels at single AZs during presynaptic homeostatic potentiation and depression. *J Neurosci* **39**, 3068–18 (2019).
33. H. Wu, S. Eno, K. Jinnai, Y. Maekawa, K. Saito, A. Abe, D. W. Williams, N. Yamagata, S. Kondo, H. Tanimoto, Octopamine signals coordinate the spatial pattern of presynaptic machineries in the Drosophila mushroom bodies. *bioRxiv*, 2024.12.02.626512 (2024).
34. P. Schlegel, Y. Yin, A. S. Bates, S. Dorkenwald, K. Eichler, P. Brooks, D. S. Han, M. Gkantia, M. dos Santos, E. J. Munnelly, G. Badalamente, L. S. Capdevila, V. A. Sane, M.

539 W. Pleijzier, I. F. M. Tamimi, C. R. Dunne, I. Salgarella, A. Javier, S. Fang, E. Perlman,
540 T. Kazimiers, S. R. Jagannathan, A. Matsliah, A. R. Sterling, S. Yu, C. E. McKellar, F.
541 Consortium, M. Costa, H. S. Seung, M. Murthy, V. Hartenstein, D. D. Bock, G. S. X. E.
542 Jefferis, A consensus cell type atlas from multiple connectomes reveals principles of
543 circuit stereotypy and variation. *bioRxiv*, 2023.06.27.546055 (2023).
544 35. A. Mrestani, M. Pauli, P. Kollmannsberger, F. Repp, R. J. Kittel, J. Eilers, S. Doose,
545 M. Sauer, A.-L. Sirén, M. Heckmann, M. M. Paul, Active zone compaction correlates with
546 presynaptic homeostatic potentiation. *Cell Rep.* **37**, 109770 (2021).
547 36. T. Ghelani, M. Escher, U. Thomas, K. Esch, J. Lützkendorf, H. Depner, M. Maglione,
548 P. Parutto, S. Gratz, T. Matkovic-Rachid, S. Ryglewski, A. M. Walter, D. Holcman, K. O.
549 Giles, M. Heine, S. J. Sigrist, Interactive nanocluster compaction of the ELKS scaffold
550 and Cacophony Ca2+ channels drives sustained active zone potentiation. *Sci. Adv.* **9**,
551 eade7804 (2023).
552 37. K. Vogt, C. Schnaitmann, K. V. Dylla, S. Knapek, Y. Aso, G. M. Rubin, H. Tanimoto,
553 Shared mushroom body circuits underlie visual and olfactory memories in Drosophila.
554 *Elife* **3**, e02395 (2014).
555 38. R. L. Davis, OLFACTORY MEMORY FORMATION IN DROSOPHILA: From
556 Molecular to Systems Neuroscience. *Annu. Rev. Neurosci.* **28**, 275–302 (2005).
557 39. J. Zirin, Y. Hu, L. Liu, D. Yang-Zhou, R. Colbeth, D. Yan, B. Ewen-Campen, R. Tao,
558 E. Vogt, S. VanNest, C. Cavers, C. Villalta, A. Comjean, J. Sun, X. Wang, Y. Jia, R. Zhu,
559 P. Peng, J. Yu, D. Shen, Y. Qiu, L. Ayisi, H. Ragoowansi, E. Fenton, S. Efrem, A. Parks,
560 K. Saito, S. Kondo, L. Perkins, S. E. Mohr, J. Ni, N. Perrimon, Large-Scale Transgenic
561 Drosophila Resource Collections for Loss- and Gain-of-Function Studies. *Genetics* **214**,
562 755–767 (2020).
563 40. E. Perisse, Y. Yin, A. C. Lin, S. Lin, W. Huetteroth, S. Waddell, Different Kenyon
564 Cell Populations Drive Learned Approach and Avoidance in Drosophila. *Neuron* **79**, 945–
565 956 (2013).
566 41. H. Amin, A. A. Apostolopoulou, R. Suárez-Grimalt, E. Vrontou, A. C. Lin, Localized
567 inhibition in the Drosophila mushroom body. *Elife* **9**, e56954 (2020).
568 42. D. Sachidanandan, A. Aravamudhan, A. Mrestani, J. Nerlich, M. Lamberty, N.
569 Hasenauer, N. Ehmann, D. Pauls, T. Seubert, I. Maiellaro, M. Selcho, M. Heckmann, S.
570 Hallermann, R. J. Kittel, Rab3 mediates cyclic AMP-dependent presynaptic plasticity and
571 olfactory learning. *bioRxiv*, 2023.12.21.572589 (2023).
572 43. N. Eckstein, A. S. Bates, A. Champion, M. Du, Y. Yin, P. Schlegel, A. K.-Y. Lu, T.
573 Rymer, S. Finley-May, T. Paterson, R. Parekh, S. Dorkenwald, A. Matsliah, S.-C. Yu, C.
574 McKellar, A. Sterling, K. Eichler, M. Costa, S. Seung, M. Murthy, V. Hartenstein, G. S.
575 X. E. Jefferis, J. Funke, Neurotransmitter classification from electron microscopy images
576 at synaptic sites in Drosophila melanogaster. *Cell* **187**, 2574-2594.e23 (2024).
577 44. C.-L. Wu, M.-F. M. Shih, P.-T. Lee, A.-S. Chiang, An Octopamine-Mushroom Body
578 Circuit Modulates the Formation of Anesthesia-Resistant Memory in Drosophila. *Curr*
579 *Biol* **23**, 2346–2354 (2013).
580 45. P.-T. Lee, H.-W. Lin, Y.-H. Chang, T.-F. Fu, J. Dubnau, J. Hirsh, T. Lee, A.-S.
581 Chiang, Serotonin–mushroom body circuit modulating the formation of anesthesia-
582 resistant memory in Drosophila. *Proc. Natl. Acad. Sci.* **108**, 13794–13799 (2011).
583 46. M. P. Nusbaum, D. M. Blitz, E. Marder, Functional consequences of neuropeptide and
584 small-molecule co-transmission. *Nat. Rev. Neurosci.* **18**, 389–403 (2017).
585 47. K. Davie, J. Janssens, D. Koldere, M. D. Waegeneer, U. Pech, Ł. Kreft, S. Aibar, S.
586 Makhzami, V. Christiaens, C. B. González-Blas, S. Poovathingal, G. Hulselmans, K. I.
587 Spanier, T. Moerman, B. Vanspauwen, S. Geurs, T. Voet, J. Lammertyn, B. Thienpont, S.

588 Liu, N. Konstantinides, M. Fiers, P. Verstreken, S. Aerts, A Single-Cell Transcriptome
589 Atlas of the Aging Drosophila Brain. *Cell* **174**, 982-998.e20 (2018).
590 48. J. Zeng, X. Li, R. Zhang, M. Lv, Y. Wang, K. Tan, X. Xia, J. Wan, M. Jing, X. Zhang,
591 Y. Li, Y. Yang, L. Wang, J. Chu, Y. Li, Y. Li, Local 5-HT signaling bi-directionally
592 regulates the coincidence time window for associative learning. *Neuron* **111**, 1118-
593 1135.e5 (2023).
594 49. F. Bilz, B. R. H. Geurten, C. E. Hancock, A. Widmann, A. Fiala, Visualization of a
595 Distributed Synaptic Memory Code in the Drosophila Brain. *Neuron* **106**, 963-976.e4
596 (2020).
597 50. A. M. Davidson, S. Kaushik, T. Hige, Dopamine-Dependent Plasticity Is
598 Heterogeneously Expressed by Presynaptic Calcium Activity across Individual Boutons of
599 the Drosophila Mushroom Body. *eNeuro* **10**, ENEURO.0275-23.2023 (2023).
600 51. N. Yamagata, T. Ezaki, T. Takahashi, H. Wu, H. Tanimoto, Presynaptic inhibition of
601 dopamine neurons controls optimistic bias. *Elife* **10**, e64907 (2021).
602 52. L. Baltruschat, L. Prisco, P. Ranft, J. S. Lauritzen, A. Fiala, D. D. Bock, G. Tavosanis,
603 Circuit reorganization in the Drosophila mushroom body calyx accompanies memory
604 consolidation. *Cell Reports* **34**, 108871 (2021).
605 53. L. Tirian, B. J. Dickson, The VT GAL4, LexA, and split-GAL4 driver line collections
606 for targeted expression in the Drosophila nervous system. *bioRxiv*, 198648 (2017).
607 54. A. Jenett, G. M. Rubin, T.-T. B. Ngo, D. Shepherd, C. Murphy, H. Dionne, B. D.
608 Pfeiffer, A. Cavallaro, D. Hall, J. Jeter, N. Iyer, D. Fetter, J. H. Hausenfluck, H. Peng, E.
609 T. Trautman, R. R. Svirskas, E. W. Myers, Z. R. Iwinski, Y. Aso, G. M. DePasquale, A.
610 Enos, P. Hulamm, S. C. B. Lam, H.-H. Li, T. R. Laverty, F. Long, L. Qu, S. D. Murphy,
611 K. Rokicki, T. Safford, K. Shaw, J. H. Simpson, A. Sowell, S. Tae, Y. Yu, C. T. Zugates,
612 A GAL4-Driver Line Resource for Drosophila Neurobiology. *Cell Rep.* **2**, 991–1001
613 (2012).
614 55. L. A. Perkins, L. Holderbaum, R. Tao, Y. Hu, R. Sopko, K. McCall, D. Yang-Zhou, I.
615 Flockhart, R. Binari, H.-S. Shim, A. Miller, A. Housden, M. Foos, S. Randkelv, C. Kelley,
616 P. Namgyal, C. Villalta, L.-P. Liu, X. Jiang, Q. Huan-Huan, X. Wang, A. Fujiyama, A.
617 Toyoda, K. Ayers, A. Blum, B. Czech, R. Neumuller, D. Yan, A. Cavallaro, K. Hibbard,
618 D. Hall, L. Cooley, G. J. Hannon, R. Lehmann, A. Parks, S. E. Mohr, R. Ueda, S. Kondo,
619 J.-Q. Ni, N. Perrimon, The Transgenic RNAi Project at Harvard Medical School:
620 Resources and Validation. *Genetics* **201**, 843–852 (2015).
621 56. S. Kondo, T. Takahashi, N. Yamagata, Y. Imanishi, H. Katow, S. Hiramatsu, K. Lynn,
622 A. Abe, A. Kumaraswamy, H. Tanimoto, Neurochemical Organization of the Drosophila
623 Brain Visualized by Endogenously Tagged Neurotransmitter Receptors. *Cell Reports* **30**,
624 284-297.e5 (2020).
625 57. M.-T. Ke, Y. Nakai, S. Fujimoto, R. Takayama, S. Yoshida, T. S. Kitajima, M. Sato,
626 T. Imai, Super-Resolution Mapping of Neuronal Circuitry With an Index-Optimized
627 Clearing Agent. *Cell Reports* **14**, 2718–2732 (2016).
628 58. D. Sage, L. Donati, F. Soulez, D. Fortun, G. Schmit, A. Seitz, R. Guiet, C. Vonesch,
629 M. Unser, DeconvolutionLab2: An open-source software for deconvolution microscopy.
630 *Methods* **115**, 28–41 (2017).
631 59. R. Haase, L. A. Royer, P. Steinbach, D. Schmidt, A. Dibrov, U. Schmidt, M. Weigert,
632 N. Maghelli, P. Tomancak, F. Jug, E. W. Myers, CLIJ: GPU-accelerated image processing
633 for everyone. *Nat. Methods* **17**, 5–6 (2020).

634

635 **Acknowledgments**

We thank all lab members of Tanimoto Lab at Tohoku University for valuable discussions.
We thank Dr. Yuki Tsukada at Keio University for crucial advice on Fiji-based image analysis.
We thank Vienna Drosophila Resource Center and Bloomington Drosophila Stock Center for transgenic flies.

Funding:
Ministry of Education, Culture, Sports, Science and Technology 22H05481 (HT)
Ministry of Education, Culture, Sports, Science and Technology 22KK0106 (HT)
Ministry of Education, Culture, Sports, Science and Technology 20H00519 (HT)
Japan Science and Technology Agency JPMJSP2114 (HW)
Tohoku University Research Program 'Frontier Research in Duo' (HT).

Author contributions:
Conceptualization: HW, HT
Methodology: HW, YM, NY, SE, SK
Investigation: HW, YM, SE
Visualization: HW, SE
Resources: SK
Supervision: HW, NY, HT
Writing—original draft: HY, HT
Writing—review & editing: HW, SE, HT

Competing interests: Authors declare that they have no competing interests.

Data and materials availability: All data are available in the main text or the supplementary materials. All imaging data and quantification results and reagents reported in this paper are available from the corresponding author upon request.

Figures and Tables

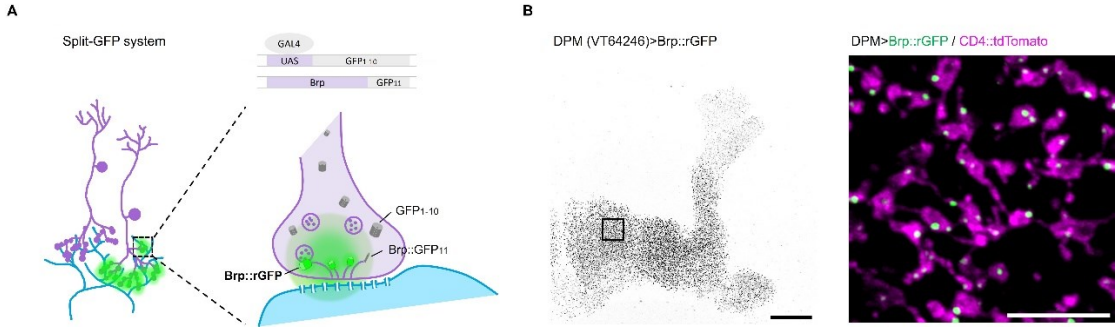

Fig. 1. Cell-type-specific visualization of endogenous presynaptic scaffold. (**A**) Schematic of the split-GFP tagging strategy. The GFP11 fragment is inserted by CRISPR/Cas9 just prior to the stop codon of *brp*, while GFP1-10 is expressed in specific cell types via GAL4-UAS system. (**B**) Brp::rGFP signals in DPM. The entire MB lobe structure is shown. The black box in the left panel indicates the zoom-in area (right panel). GFP1-10 and CD4::tdTomato (magenta) were co-expressed using VT64246-GAL4. Scale bar, 20 μm (left); 5 μm (right).

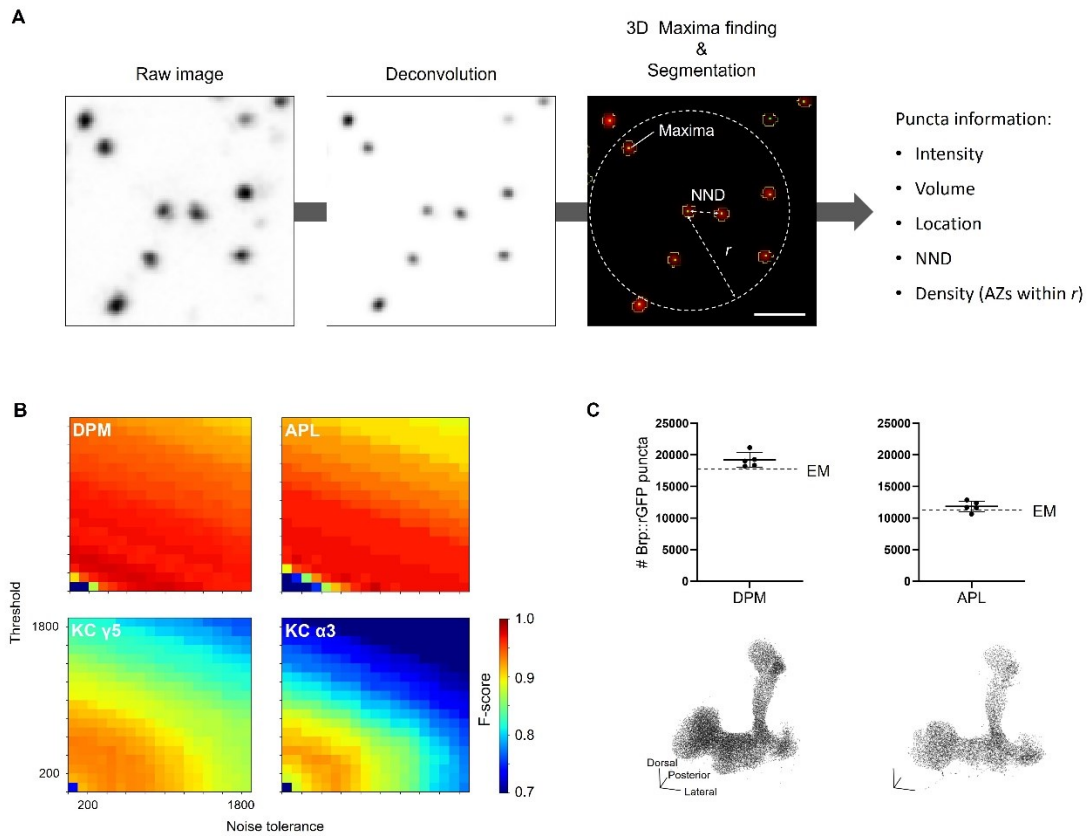

Fig. 2. Spatial characterization of Brp::rGFP clusters at single-AZ level. (**A**) Image processing pipeline. Raw images were processed with image deconvolution to improve the signal quality. 3D maxima (green pixels) are detected for each Brp::rGFP cluster. Pixels around the maxima were clustered and used to created 3D ROIs, indicated by yellow circles. Brp::rGFP intensity, cluster volume and location were recorded. The mean nearest neighbor distance (NND) was determined for each sample, with *r* set to 3 × mean NND. The "AZ density" is the number of Brp::rGFP clusters within *r*. (**B**) Heatmaps of F-scores showing the detection performance across in different cell types. An intensity threshold (threshold) is applied to reduce the background noise when detecting 3D maxima. The noise tolerance is the parameter that adjusts the sensitivity of 3D maxima detection. The color represents the F-score value. (**C**) Number of Brp::rGFP clusters detected in DPM and APL. The dashed lines indicate the number of electron dense projections identified in the hemibrain connectome for DPM (17530) and APL (10789) on the MB lobes and peduncle. For both DPM and APL, n = 5. Lower panels show the representative 3D reconstructions of Brp::rGFP clusters in DPM and APL. Scale bars, 20 µm. Data were presented as mean ± s.e.m.

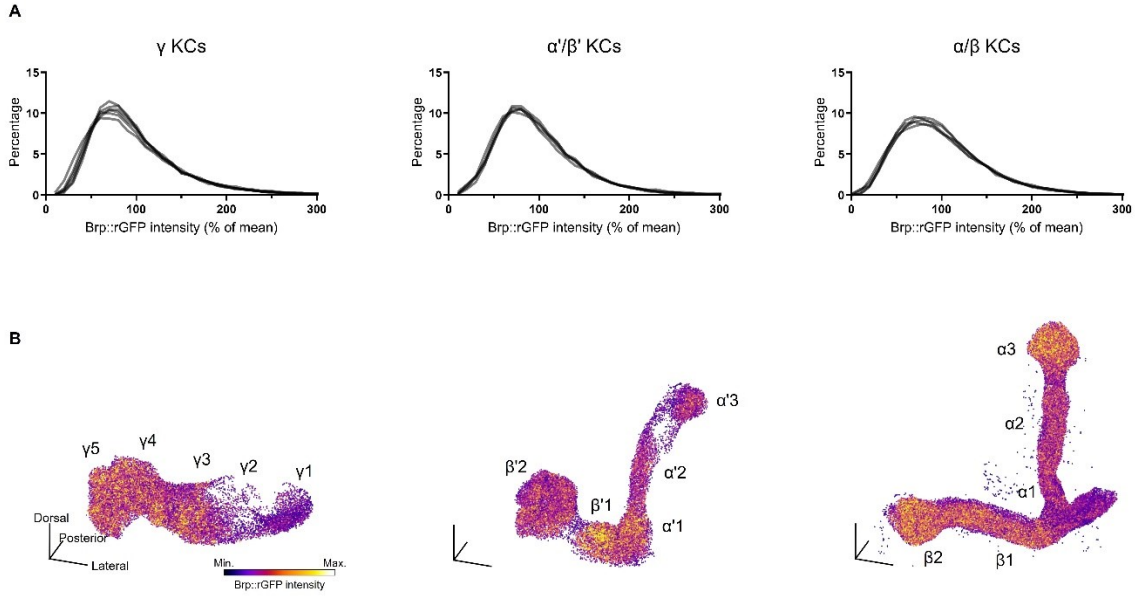

Fig. 3. Compartmentalized AZ structures of KCs. (**A**) Histograms of Brp::rGFP intensity of individual AZs from three KC subtypes. The intensity value is normalized by the average value of each data set (each sample). Each line represents the histogram of one independent sample. γ KCs (MB009B-GAL4), n = 6; α/β KCs (MB370B-GAL4), n = 5; α'/β' KCs (MB008B-GAL4), n = 5. (**B**) 3D reconstructions of Brp::rGFP clusters in three KC subtypes, colored by the Brp::rGFP intensity. The approximate locations of compartments are as indicated. Min. and Max. were set to represent the lowest and highest 5% of Brp::rGFP intensity value in the dataset respectively. Scale bars, 20 μm.

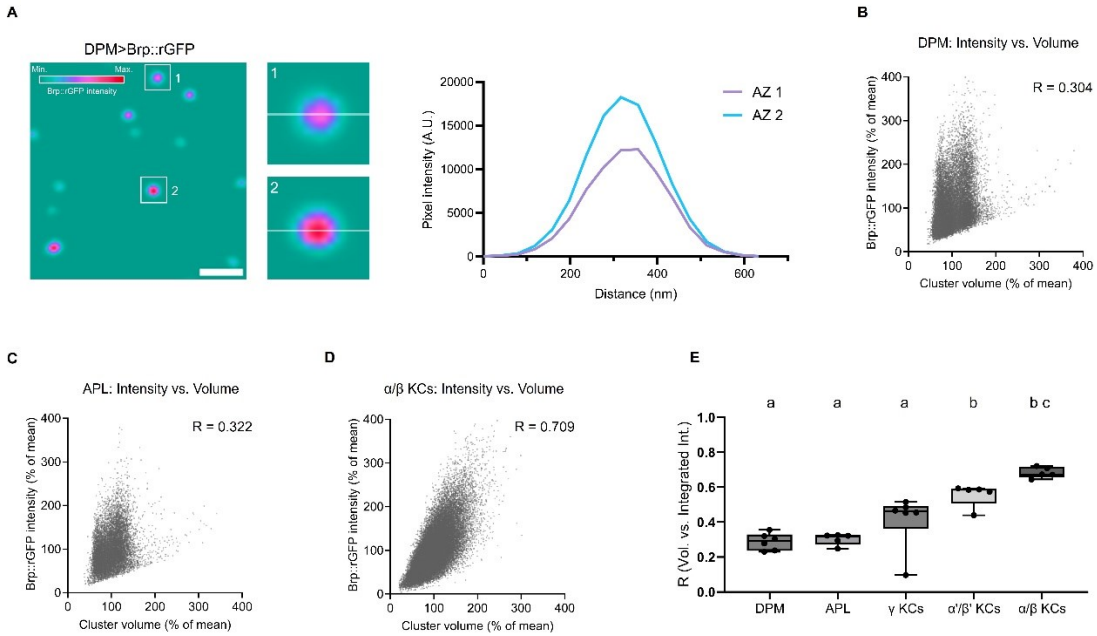

Fig. 4. The variability of Brp::rGFP density depends on cell type.
(**A**) Brp::rGFP clusters with distinct intensities but similar size in DPM. The left panel shows a cropped image of Brp::rGFP in DPM. White boxes indicate areas zoomed-in in panels 1 and 2. Transparent white lines in panels 1 and 2 show the lines on which the intensity profiles were plotted. Intensity profiles were plotted for AZ1 (magenta) and AZ2 (blue) respectively. (**B-D**) Scatter plots showing the correlation between the Brp::rGFP intensity and cluster volume in DPM, APL and α/β KCs. Data of three representative

samples were shown. Pearson correlation coefficient R were calculated for each sample. (**E**) Correlations between Brp::rGFP intensity and cluster volume in different cell types. DPM (n = 6), APL (n = 5), γ KCs (n = 6, MB009B-GAL4), α'/β' KCs (n = 5, MB370B-GAL4), α/β KCs (n = 5, MB008B-GAL4). Kruskal-Wallis test with original False Discovery Rate (FDR) method of Benjamini and Hochberg correction. DPM vs. α'/β' KCs: P = 0.0253; DPM vs. α/β KCs: P = 0.0009; APL vs. α/β KCs: P = 0.0035; γ KCs vs. α/β KCs: P = 0.0418. Kruskal-Wallis test. Values marked with different lowercase letters represent significant difference (P < 0.05); Data were presented as box plots showing center (median), whiskers (Min. to Max.).

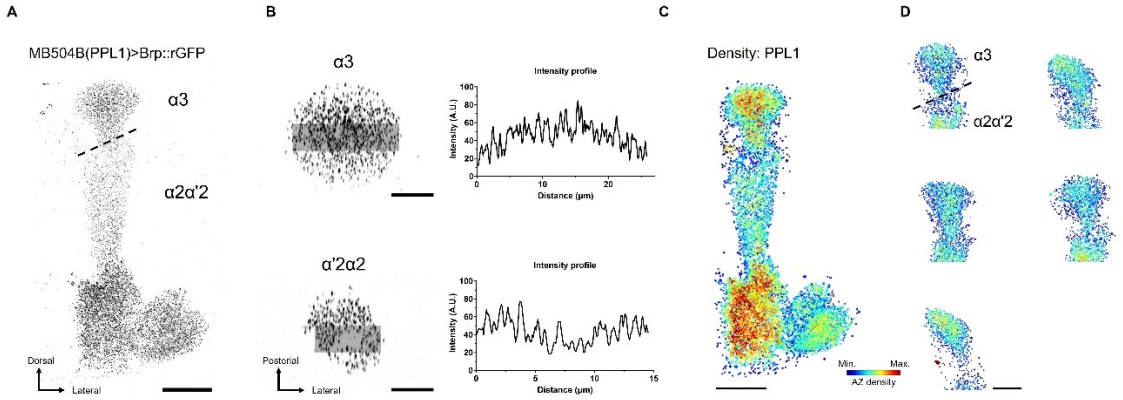

Fig. 5. Stereotyped AZ distribution of PPL1-α3 DAN. (**A**) Brp::rGFP in PPL1 DANs. UAS-GFP1-10 was expressed using MB504B-GAL4. Dashed line marks the rough boundary between α3 and α2α'2 compartments. Scale bar, 20 μm. (**B**) Brp::rGFP intensity profiles of α3 and α2α'2 compartments. Left panels show the max-projection images of α3 and α2α'2 optical coronal sections. Transparent gray stripes indicate areas where intensity profiles are plotted in the right panels. Scale bars, 10 μm. (**C**) 3D reconstruction colored by the AZ density in PPL-1 DANs. Color scale: Min. = 0, Max. = 40. Dashed line indicates the rough boundary between α3 and α2α'2 compartments. Scale bar, 20 μm. (**D**) Stereotyped AZ distribution pattern in PPL1-α3 across individuals. 3D reconstructions show the AZ density across different brain samples. Scale bar, 20 μm.

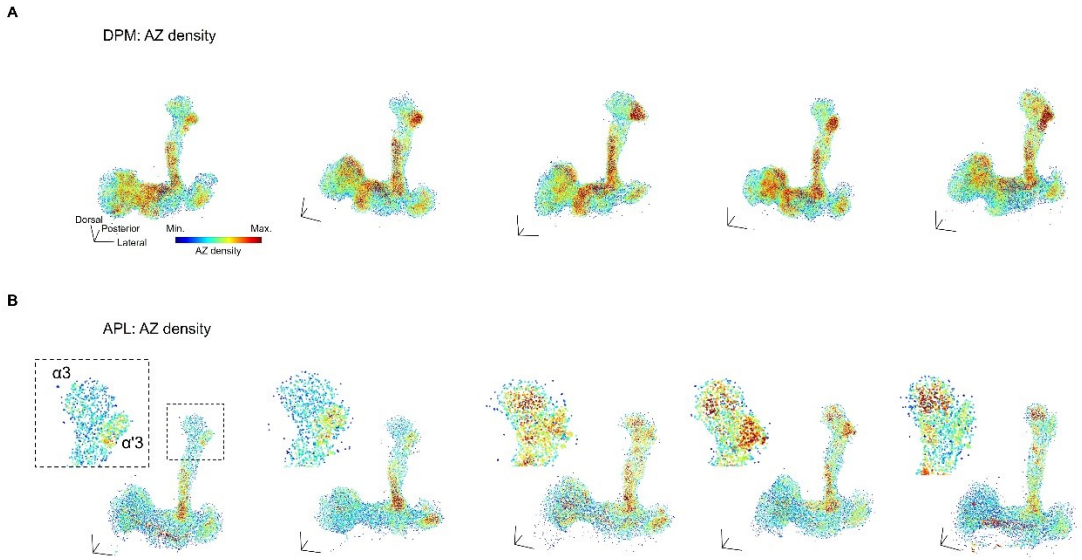

Fig. 6. Cell-type-specific stereotypy of AZ spatial distributions.
(**A**) 3D reconstructions of Brp::rGFP clusters in DPMs, colored by AZ density. Color scale: Min. = 0, Max. = 35. Black arrows indicate consistently high AZ density regions across brain samples. Scale bars, 20 μm. (**B**) 3D reconstructions of Brp::rGFP clusters in APLs, colored by AZ density. Color scale: Min. = 0, Max. = 30. Black dashed square indicates the area zoomed-in. APL reconstructions are arranged from left to right according to the overall AZ density in α3.

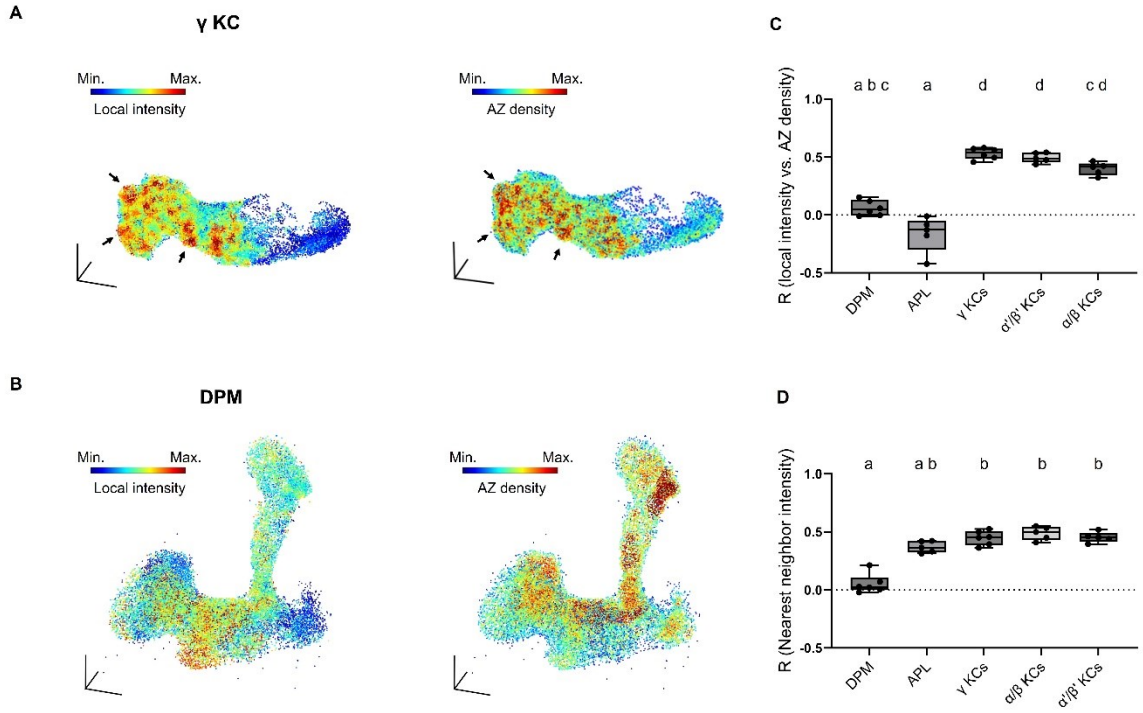

Fig. 7. Local intensity analysis revealed sub-compartmental AZ structures. (**A**) 3D reconstructions of Brp::rGFP clusters in a γ KC sample, colored by local intensity and AZ density. Black arrows indicate areas with both high local intensities and high AZ densities. Min. and Max. were set to represent the lowest and highest 5% in local intensity value respectively. Color scale of AZ density: Min. = 0 and Max = 35. (**B**) 3D reconstructions of Brp::rGFP clusters in a DPM neuron, colored by local intensity and AZ density. Min. and Max. are set to represent the lowest and highest 5% in local intensity value respectively. Color scale of AZ density: Min. = 0, Max. = 35. (**C**) Correlations between AZ density and local intensity in different cell types. DPM (n = 6), APL (n = 5), γ KCs (n = 6, MB009B-GAL4), α'/β' KCs (n = 5, MB370B-GAL4), α/β KCs (n = 5, MB008B-GAL4). DPM vs. γ KCs: P = 0.0171; DPM vs. α'/β' KCs: P = 0.0171; APL vs. γ KCs: P = 0.0014; APL vs. α'/β' KCs: P = 0.0014; APL vs. α/β KCs: P = 0.0171; (**D**) Correlations of Brp::rGFP intensities between nearest neighbor AZs in different cell types. Brp::rGFP intensities were log transformed. DPM vs. γ KCs: P = 0.0066; DPM vs. α'/β' KCs: P = 0.0027; DPM vs. α/β KCs: P = 0.0066; Scale bar: 1 μm.

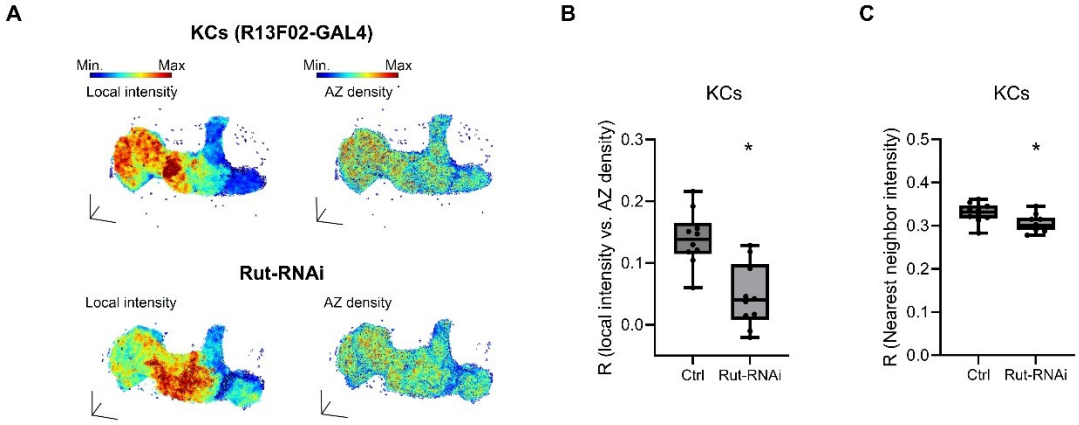

Fig. 8. Local AZ structures in KCs are Rut-dependent. (**A**) Decorrelation of AZ hot spots by knocking-down Rut. (**B**) Knocking-down Rut decreased the correlation between AZ density and local intensity in KCs. P = 0.0007. Brp::rGFP was visualized using R13F02-GAL4. Signals were sampled from all MB compartments. (**C**) Knocking-down Rut decreased the correlation of Brp::rGFP intensities between nearest neighbor AZs in KCs. P = 0.0355. Mann Whitnet test *P < 0.05. Data were presented as box plots showing centre (median), whiskers (Min. to Max.).